



Article

Dual-Activated Nano-Prodrug for Chemo-Photodynamic Combination Therapy of Breast Cancer

Ziyao Lu ^{1,2,†}, Gan Xu ^{3,†}, Xiaozhen Yang ³, Shijia Liu ¹, Yang Sun ^{1,4}, Li Chen ^{1,2}, Qinying Liu ^{1,*}
and Jianyong Liu ^{3,5,6,*} 

- ¹ Fujian Provincial Key Laboratory of Tumor Biotherapy, Clinical Oncology School of Fujian Medical University, Fujian Cancer Hospital, Fuzhou 350014, China
 - ² Fujian Provincial Key Laboratory of Medical Instrument and Pharmaceutical Technology, College of Biological Science and Technology, Fuzhou University, Fuzhou 350108, China
 - ³ National & Local Joint Biomedical Engineering Research Center on Photodynamic Technologies, College of Chemistry, Fuzhou University, Fuzhou 350108, China
 - ⁴ Department of Gynecology, Clinical Oncology School of Fujian Medical University, Fujian Cancer Hospital, Fuzhou 350014, China
 - ⁵ Key Laboratory of Molecule Synthesis and Function Discovery, Fujian Province University, College of Chemistry, Fuzhou University, Fuzhou 350108, China
 - ⁶ State Key Laboratory of Photocatalysis on Energy and Environment, College of Chemistry, Fuzhou University, Fuzhou 350108, China
- * Correspondence: liuqy@fjmu.edu.cn (Q.L.); lkxw82@fzu.edu.cn (J.L.)
† These authors contributed equally to this work.



Citation: Lu, Z.; Xu, G.; Yang, X.; Liu, S.; Sun, Y.; Chen, L.; Liu, Q.; Liu, J. Dual-Activated Nano-Prodrug for Chemo-Photodynamic Combination Therapy of Breast Cancer. *Int. J. Mol. Sci.* **2022**, *23*, 15656. <https://doi.org/10.3390/ijms232415656>

Academic Editors: Antonino Mazzaglia, Angela Scala and Enrico Caruso

Received: 20 October 2022

Accepted: 7 December 2022

Published: 10 December 2022

Publisher's Note: MDPI stays neutral with regard to jurisdictional claims in published maps and institutional affiliations.



Copyright: © 2022 by the authors. Licensee MDPI, Basel, Switzerland. This article is an open access article distributed under the terms and conditions of the Creative Commons Attribution (CC BY) license (<https://creativecommons.org/licenses/by/4.0/>).

Abstract: Herein, we developed a dual-activated prodrug, BTC, that contains three functional components: a glutathione (GSH)-responsive BODIPY-based photosensitizer with a photoinduced electron transfer (PET) effect between BODIPY and the 2,4-dinitrobenzenesulfonate (DNBS) group, and an ROS-responsive thioketal linker connecting BODIPY and the chemotherapeutic agent camptothecin (CPT). Interestingly, CPT displayed low toxicity because the active site of CPT was modified by the BODIPY-based macrocycle. Additionally, BTC was encapsulated with the amphiphilic polymer DSPE-mPEG₂₀₀₀ to improve drug solubility and tumor selectivity. The resulting nano-prodrug passively targeted tumor cells through enhanced permeability and retention (EPR) effects, and then the photosensitizing ability of the BODIPY dye was restored by removing the DNBS group with the high concentration of GSH in tumor cells. Light-triggered ROS from activated BODIPY can not only induce apoptosis or necrosis of tumor cells but also sever the thioketal linker to release CPT, achieving the combination treatment of selective photodynamic therapy and chemotherapy. The antitumor activity of the prodrug has been demonstrated in mouse mammary carcinoma 4T1 and human breast cancer MCF-7 cell lines and 4T1 tumor-bearing mice.

Keywords: nano-prodrug; photodynamic therapy; reactive oxygen species; activation; combination therapy

1. Introduction

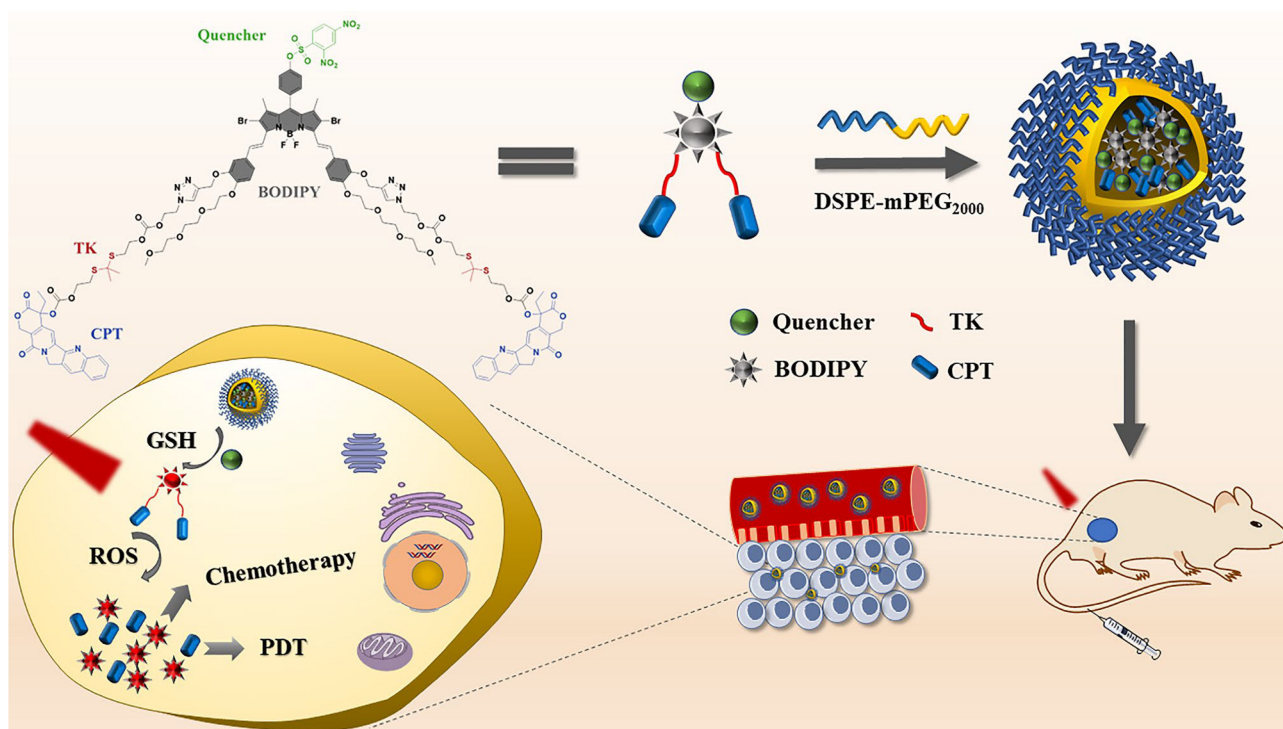
Cancer has become one of the most important causes of death in the past few decades due to invasion and metastasis [1,2]. Although chemotherapy has always been a powerful tool to induce apoptosis or necrosis of cancer cells [3,4], it has limited effects due to its low selectivity and serious systemic toxicity [5]. Therefore, there is an urgent need to develop antitumor drugs with low toxicity and high efficiency.

Photodynamic therapy (PDT) is regarded as one of the most effective treatments for cancer due to its small trauma [6], poor toxicity and high spatiotemporal selectivity [7,8]. PDT contains three critical components, including a photosensitizer (PS), light with a specific wavelength and oxygen to generate reactive oxygen species (ROS), particularly singlet oxygen, to induce cell apoptosis or necrosis [9]. Pioneering studies have confirmed

that the combination of PDT and chemotherapy is a promising treatment mode, which not only reduces the dose of the most toxic component but also overcomes single-mode limitations [10,11]. However, most encapsulation or conjugation of PSs and chemotherapeutic agents typically result in drug leakage and low drug toxicity [12,13]. An effective method has been developed to overcome the above shortcomings and improve drug biological activity. Specifically, chemotherapeutic agents are activated by internal (such as hypoxia, high concentrations of GSH, etc.) or external (such as temperature, ROS, etc.) stimuli to release on-demand drugs [14,15]. Youngjae You et al. linked phthalocyanine to PTX using a ROS-sensitive linker. ROS produced after illumination can be used to kill cancer cells as well as cut off the linker to release PTX [16,17]. However, prodrugs can still cause phototoxicity and side effects to normal cells due to their poor selectivity and irregular tumor margins [18,19]. Thus, more practical PSs that only work in tumor tissue through activation by the tumor environment have emerged.

Compared with the normal cell microenvironment, tumor cells have some inimitable pathological signals, such as vascular abnormalities, high concentrations of GSH, acidosis and hypoxia [20–23]. The PSs lose their photoactivity by connecting to quenchable groups through chemical bonds sensitive to the tumor microenvironment. In the tumor microenvironment, the chemical bonds break, the quenchable effect disappears and the photoactivity of PSs recovers [24–26]. There are many types of intermolecular quenching mechanisms, such as photoinduced electron transfer (PET) [27,28], forster resonance energy transfer (FRET) [29,30] and internal charge transfer (ICT) [31,32]. Akkaya et al. designed a GSH-activated BODIPY based on the PET effect between the 2,4-dinitrobenzenesulfonate (DNBS) group and the parent nucleus of BODIPY [33]. Zheng et al. designed an MMP-7-responsive PS in which porphyrin and a quenching agent (BHQ3) could cause the FRET effect [34]. Zhao et al. designed an activated PS based on the ICT effect between the DNBS group and iodinated BODIPY [35]. Although environmentally responsive PSs avoid damage to normal tissues, nontargeting agents still lead to low PDT efficiency [36,37]. To solve the above drawback, specific chemical bonds are usually added to PSs to connect polypeptides, vitamins, antibodies and small molecules, which increase tumor targeting [38–42]. Alternatively, taking advantage of the large space between vascular endothelial cells at the tumor, nanoparticles loaded into PSs also enter the tumor tissue by virtue of the enhanced permeability and retention (EPR) effect [43–46].

In this study, we designed a prodrug that combines passive targeting and stepwise activation. First, the fluorescence of BODIPY was quenched due to the PET effect existing between BODIPY and the DNBS group. In an environment of high concentration GSH, the sulfhydryl group of GSH and the nitro sulfonate structure undergo a nucleophilic substitution reaction which leaves the 2,4-dinitrobenzenesulfonyl moiety, the PET effect is inhibited and the fluorescence of BODIPY is restored. Then, CPT is attached to BODIPY by means of a ROS-sensitive linker. The fluorescence of CPT is quenched by BODIPY derivatives, accounting for FRET, and the low toxicity of CPT is displayed because the active site of CPT is modified by a BODIPY-based macrocycle. Meanwhile, nanoparticles are coated with the amphiphilic polymer DSPE-mPEG₂₀₀₀ to improve drug solubility and tumor selectivity. As demonstrated in Scheme 1, after entering the tumor through passive targeting, the prodrug is activated by a high concentration of GSH in the tumor, and ROS is produced under light stimulation to damage tumor cells. Meanwhile, ROS ruptures the TK linker between BODIPY and CPT, releasing CPT to achieve the combination treatment of selective PDT and chemotherapy.



Scheme 1. The chemical structure and activation mechanism of nano-prodrug BTC NPs.

2. Results and Discussion

2.1. Molecular Design and Synthesis

In this paper, we rationally designed GSH and a ROS-responsive prodrug that consists of the DNBS group, BODIPY-based PS, a ROS-cleavable thioketal linker and CPT. As is known, the BODIPY-based fluorescent dye is a hopeful fluorescent chromophore, which is mainly due to its strong absorption in the visible and near infrared region (NIR), and robust photo-stability. Interestingly, its spectral properties can be significantly tuned by reasonable chemical modification. Scheme 2 depicts the synthetic route for the BTC. First, the distyryl-substituted BODIPY **1** was modified with the 3,4-dinitrobenzenesulfonyl chloride to produce GSH-responsive BODIPY **2**. Owing to photo-induced electron transfer (PET), GSH-responsive BODIPY **2** had a relatively weak fluorescence emission and a red-shift absorption, which is beneficial to the PDT of deep tissues. Then, BODIPY **2** was clicked with covalent CPT **3a** containing a ROS-sensitive linkage to attain BTC. For comparison, the reference compounds with ROS-insensitive carbon chains, BCC was also prepared in a similar procedure. In brief, BTC and BCC were nontoxic to healthy cells with or without light. In contrast, BCC only restored phototoxicity in tumor cells with a laser. However, BTC restored phototoxicity and chemotoxicity. The synthesis process and characterization in the Supporting Information demonstrate that BTC and BCC were successfully obtained (Figures S12–S17).

2.2. Photophysical and Photochemical Properties

2.2.1. Photophysical Properties

The electronic absorption spectra of BTC, BCC, BODIPY **2** and CPT were measured in dimethylsulfoxide (DMSO). As shown in Figures S1 and S2, BTC, BCC and BODIPY **2** showed a strong Q band with a maximum absorption wavelength of 683 nm. It was found that the maximum absorption wavelength of BODIPY **2** was redshifted by 10 nm compared with that of BODIPY **1** (Table S1), which may have been due to the strong electron-absorbing effect of introducing the DNBS group. In addition, the absorption of BTC and BCC were the superposition of CPT and BODIPY **2**, which indicated that the introduction of CPT negligibly affected the electron absorption of BTC and BCC (Figure S1). When BODIPY **1**

circulation; however, once they enter the tumor cells, they can be activated rapidly by GSH inside the tumor cells.

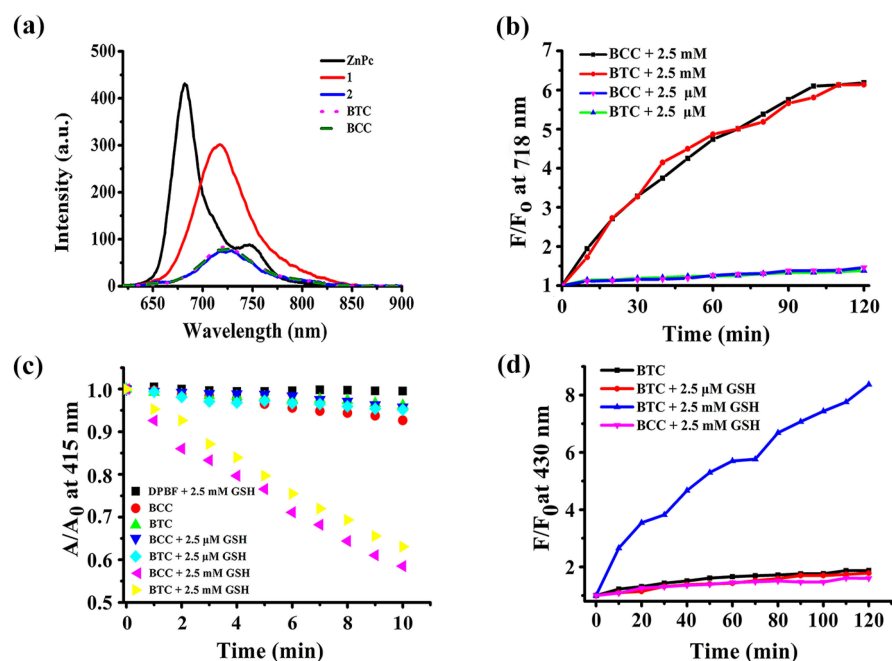


Figure 1. (a) Fluorescence emission spectra of ZnPc, 1, 2, BCC, and BTC with absorbances between 0.04–0.05 at 610 nm in DMSO ($\lambda_{\text{exc}} = 610$ nm). (b) Changes in fluorescence intensity of BTC and BCC at 718 nm with culture time in DMSO/PBS (3:1, *v/v*) after addition of GSH (2.5 μM or 2.5 mM). (c) Comparison of the degradation rates of DPBF as monitored by the decrease in electronic absorbance at 415 nm with irradiation (660 nm, 1 mW/cm^2) time in DMSO/PBS (3:1, *v/v*) under various conditions. (d) Changes in fluorescence intensity of BTC and BCC at 430 nm with irradiation (660 nm, 30 mW/cm^2) time in DMSO/PBS (3:1, *v/v*) after treatment with GSH (2.5 μM or 2.5 mM) for 2 h.

As expected, the singlet oxygen ($^1\text{O}_2$) generation efficiency of BTC and BCC also responded similarly. The trapping agent of singlet oxygen, 1,3-diphenyliso-benzofuran (DPBF), is the best choice for singlet oxygen detection due to its high stability and sensitivity. When the $^1\text{O}_2$ reacts with DPBF in solution, the conjugated structure of DPBF will be destroyed and the absorption of DPBF at 415 nm will be reduced. Therefore, the $^1\text{O}_2$ production capacity of the compound was indirectly reflected by observing the decrease rate of DPBF absorption at 415 nm. As depicted in Figure S4b,e, there were no considerable absorption changes for DPBF at 415 nm in the presence of BTC and BCC under light (660 nm, 1 mW/cm^2). The results indicated that both BTC and BCC did not effectively generate singlet oxygen. Under 2.5 μM GSH, there was essentially unchanged absorbance of DPBF at 415 nm under irradiation at 660 nm (Figures 1c and S4c,f), which indicated that BTC and BCC could not effectively generate singlet oxygen after coculturing for 120 min with 2.5 μM GSH. However, after incubating these two compounds with 2.5 mM GSH, the absorbance of DPBF at 415 nm decreased remarkably (Figures 1c and S4d,g), indicating that these two compounds obviously boosted the photo-degradation of DPBF. All the above findings revealed that the intramolecular PET process in BTC and BCC disappeared with the high concentration of GSH, increasing the fluorescence emission and singlet oxygen generation efficiency.

2.2.3. ROS-Triggered CPT Release

The first step was to confirm the intramolecular FRET process in BTC and BCC. The fluorescence of BTC or BCC was compared with that of CPT under the same conditions. Upon excitation at 370 nm, the fluorescence of CPT was strong at 430 nm (Figure S5). By contrast, we found that the fluorescence intensity of BTC and BCC decreased dramatically

at 430 nm, and a new fluorescence peak appeared at 724 nm (Figure S5). This phenomenon accounted for the FRET effect between BODIPY units and CPT, such that the fluorescence of CPT was quenched by BODIPY units. The next step was to evaluate the CPT moiety release in the prodrug BTC by monitoring the fluorescence changes at 430 nm under different conditions. According to Figures 1d and S6a, after the treatment of the solution of BTC with laser light (660 nm, 30 mW/cm²), the fluorescence intensity of CPT hardly changed, indicating the CPT moiety was barely released. After pretreating with 2.5 μM of GSH for 120 min, the fluorescence emission of CPT moiety from BTC was insignificant under laser irradiation (660 nm, 30 mW/cm²) (Figure S6b). By contrast, after treatment with 2.5 mM GSH for 120 min (Figures 1d and S6c), the fluorescence of CPT in the solution increased significantly and reached a plateau under light (660 nm, 30 mW/cm²). Due to the fluorescence of the CPT moiety in BTC being in the “off” state through the FRET process, the increased fluorescence intensity at 430 nm was attributed to the released CPT from BTC. Furthermore, the fluorescence of CPT could not enhance the reference BCC upon irradiation after the treatment with 2.5 mM GSH (Figures 1d and S6d).

2.3. Preparation and Characterization of BTC NPs and BCC NPs

Since BTC and BCC are water-insoluble, we wrapped BTC and BCC into soluble nanoparticles by using the amphiphilic polymer DSPE-mPEG₂₀₀₀, which can increase drug solubility but can also improve tumor targeting through the EPR effect. The hydrodynamic diameters of BTC NPs and BCC NPs were 99.7 nm and 112.5 nm, respectively, and the polydispersity index (PDI) of BTC NPs and BCC NPs were approximately 0.2 (Figures 2a and S7a), showing a promising distribution in solution. Transmission electron microscopy (TEM) results showed that the BTC NPs and BCC NPs had uniform and monodispersed spherical shapes. Additionally, the loading content and loading efficiency of BTC (BCC) in the BTC NPs (BCC NPs) were 1.5% (1.3%), and 85% (80%), respectively. The BTC NPs and the BCC NPs also showed superior stability in an aqueous solution, and no precipitation or significant changes in average size were observed within 7 days (Figures 2b and S7b), which guaranteed their potential application in vivo. We found that the maximum absorption wavelength of the BTC NPs and BCC NPs was lower than those of BTC and BCC, which confirmed the BTC NPs and BCC NPs have aggregation (Figures 2c and S7c). Upon excitation at 640 nm, both NPs emitted a negligible fluorescence (Figures 2d and S7d), which indicated that aggregation favored quenching the fluorescence.

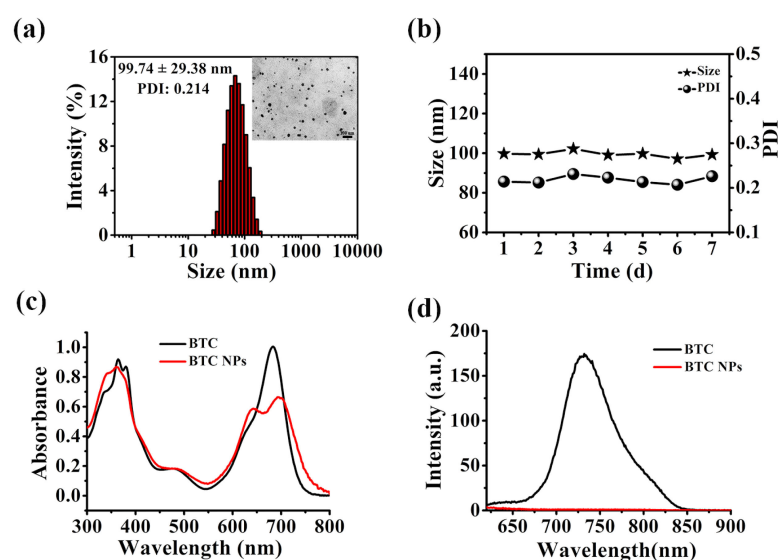


Figure 2. (a) Dynamic light scattering and transmission electron microscope images of BTC NPs. (b) Changes in particle size and PDI in PBS for 7 days. (c) UV-vis absorption spectra of BTC in DMSO and BTC NPs in PBS (both at 10 μM). (d) Fluorescence emission spectra of BTC in DMSO and BTC NPs in PBS (both at 10 μM).

2.4. In Vitro Assessments

2.4.1. GSH-Responsive Intracellular Fluorescence

The activation effect of BTC NPs in mouse mammary carcinoma 4T1 and human breast cancer MCF-7 cell lines was also monitored to estimate the intracellular fluorescence of BDP units via confocal laser scanning microscopy (CLSM). According to Figures 3a,c and S8a,c, both the BTC NPs and BCC NPs showed bright intracellular fluorescence in treated 4T1 and MCF-7 cells, indicating that the nanoparticles could be activated by GSH in tumor cells. In contrast, the intracellular fluorescence intensity of the BTC NPs and BCC NPs decreased significantly after the tumor cells were pretreated with L-buthionine sulfoximine (BSO) to deplete intracellular GSH [47], which indicated that GSH inside the tumor cells should be the key to activating the fluorescence emission of the BTC NPs and BCC NPs.

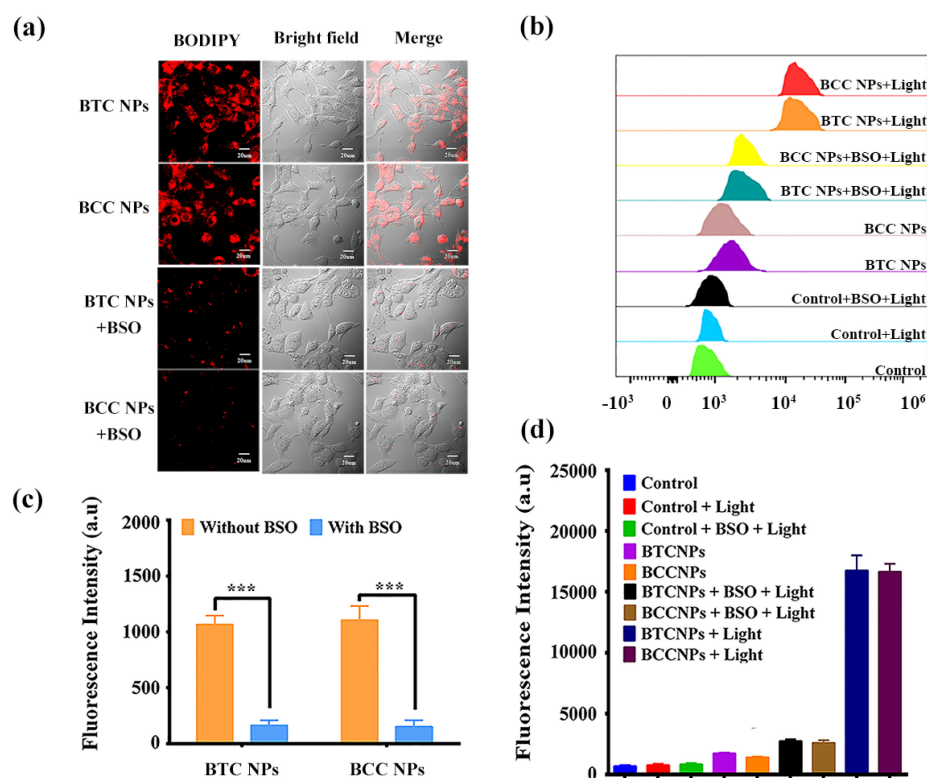


Figure 3. (a) CLSM images of 4T1 cells after incubation with the BTC NPs and BCC NPs (5 µM) for 24 h, or cells pretreated with BSO (10 mM) for 12 h. (b) ROS evaluation of BTC NPs and BCC NPs in 4T1 cells under light irradiation at 660 nm (20 mW/cm², 5 min) by flow cytometry. (c) Quantitative results of (a) (***) ($p < 0.001$). (d) Quantitative results of (b).

2.4.2. Intracellular ROS Level

Since ROS produced by PSs can directly kill tumor cells, the ROS generation ability of PSs in tumor cells is extremely important. Here, the release of CPT was also controlled by the ROS. Next, we investigated ROS generation in 4T1 and MCF-7 cells using 2,7-dichlorofluorescein yellow diacetate (DCFH-DA) as the ROS indicator. After DCFH-DA enters cells through diffusion, DCFH is rapidly oxidized by intracellular ROS and then generates DCF with strong fluorescence, which can be detected by flow cytometry. There was negligible fluorescence in 4T1 (Figure 3b,d) and MCF-7 cells (Figure S8b,d) treated with PBS with or without light at 660 nm, indicating that the content of endogenous ROS in cells was relatively low. When the BTC NPs- and BCC NPs-treated cells were stimulated with a laser at 660 nm, the fluorescence was markedly enhanced and was 5-fold higher than that without laser stimulation. The results implied that nanoparticles could be activated by intracellular GSH and produced large amounts of ROS under light. We also investigated whether ROS could still be produced by the nanoparticles when intracellular

GSH was depleted. As the results showed, when cells were pretreated with BSO followed by the BTC NPs and BCC NPs, the intracellular fluorescence of DCF was significantly weakened, demonstrating that BSO reduced the intracellular concentration of GSH, leading the prodrug to inactivate.

2.4.3. Intracellular CPT Release

We further evaluated the release efficiency of CPT from the BTC NPs triggered by light at the cellular level by CLSM. After treatment with BTC NPs for 24 h, there was only negligible blue fluorescence in the CPT channel in 4T1 (Figure 4a,c,d) and MCF-7 cells (Figure S9a–c). However, the fluorescence of CPT was significantly enhanced when illuminated at 660 nm for 2 min, demonstrating the release of CPT from the BTC NPs under light. Moreover, regardless of the light, the fluorescence of CPT from the BCC NPs was very minimal due to the absence of an ROS-cleavable linker. Notably, when the cells were treated with the BTC NPs or BCC NPs, the red fluorescence in the BODIPY channel of the laser group was similar to that of the no-laser group.

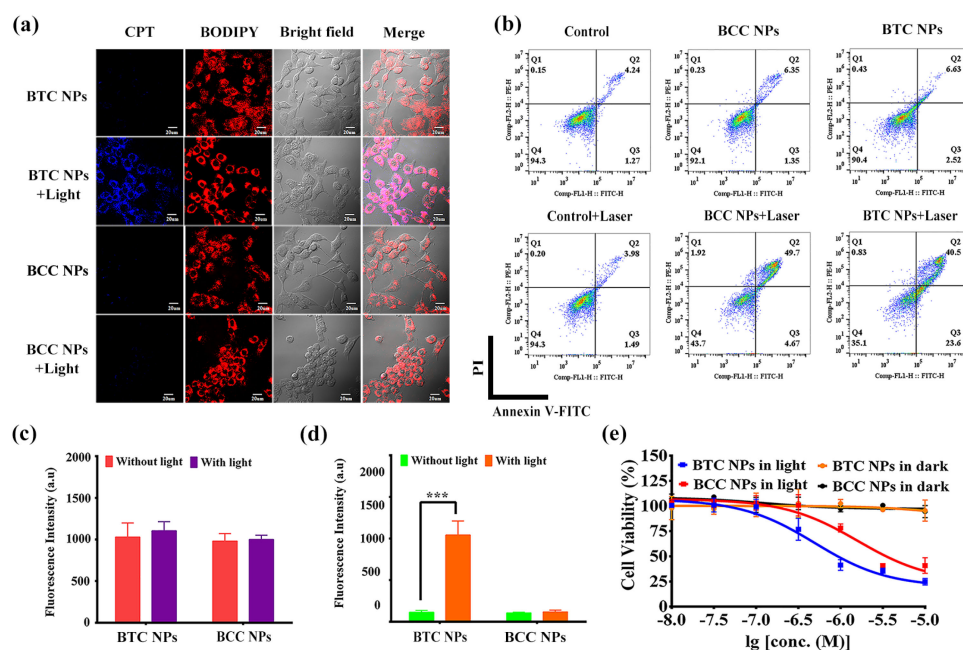


Figure 4. (a) CLSM images of 4T1 cells treated with BTC NPs (or BCC NPs) (5 μ M) in the presence/absence of light illumination (660 nm, 20 mW/cm², 2 min). (b) Flow cytometry analysis for 4T1 cells incubated with BTC NPs (or BCC NPs) (5 μ M) with or without light (20 mW/cm², 5 min). (c) Quantitative results of (a) for average fluorescence intensity of BODIPY moiety in 4T1 cells. (d) Quantitative results of (a) for average fluorescence intensity of CPT moiety in 4T1 cells. (***) $p < 0.001$. (e) Cytotoxic effects of BTC NPs (or BCC NPs) against 4T1 cells in the absence and presence of light (660 nm, 20 mW/cm², 5 min); Data are expressed as mean \pm SD of three independent experiments, each performed in sextuplicate.

2.4.4. Cytotoxicity Assays

To explore the killing activity of nanoparticles on tumor cells directly, the cytotoxicities of the BTC NPs and BCC NPs were investigated in 4T1 and MCF-7 cells by methyl thiazolyl tetrazolium (MTT) assays. In Figures 4e and S9d, the BTC NPs and BCC NPs exhibited negligible dark toxicity, even at a concentration of 10 μ M. The results indicated the cytotoxicity of CPT was largely inhibited by conjugating with BODIPY-based PSs. However, following laser exposure, the half maximal inhibitory concentrations (IC₅₀) values for the BTC NPs were decreased to 0.50 μ M for 4T1 cells and 0.63 μ M for MCF-7 cells, which were lower than the BCC NPs (1.6 and 1.5 μ M, respectively). The cytotoxicity differences between the BTC NPs and the BCC NPs were probably because the BTC NPs killed the tumor cells by ROS

and ROS-triggered release of CPT in a combination treatment of PDT and chemotherapy, while the BCC NPs damaged the tumor cells only by ROS via PDT treatment. Furthermore, we detected the cell apoptosis induced by the BTC NPs and the BCC NPs by an Annexin V-FITC/PI Apoptosis Kit. As shown in Figure 4b, both the BTC NPs and BCC NPs induced obvious apoptosis under light conditions, but the apoptosis rate induced by the BTC NPs was higher than that induced by the BCC NPs, which suggested that the BTC NPs could kill tumor cells more efficiently through the combination of PDT and chemotherapy.

2.5. *In Vivo* Studies

The biodistribution of the BTC NPs in tumor tissues was evaluated in 4T1 tumor-bearing BALB/c mice. Because BODIPY-based PSs could emit near-infrared (NIR) fluorescence, the time-dependent accumulation process of the BTC NPs was directly observed by fluorescence molecular tomography (FMT). As shown in Figure 5a, there was a fluorescence signal for mice after tail vein injection with the BCC NPs and BTC NPs for 4 h. The fluorescence signal increased first and then decreased, and the maximum accumulation time of BCC NPs and BTC NPs was 12 h. This was because of the EPR effect of the nano-prodrug which caused pronounced tumor enrichment of BCC NPs and BTC NPs; the nano-prodrug was further activated by high concentrations of GSH in the tumor tissues. Furthermore, BCC and BTC displayed weak fluorescence signals at the tumor sites (Figure S10a), which was due to poor tumor accumulation. We further collected tumor tissue and other main organs to analyze the prodrug distribution at the maximum accumulation time and found that the concentrations of the BCC NPs and BTC NPs in tumor tissue were much higher than that in other main organs (Figure 5b), suggesting that the nano-prodrug could target tumor tissues. Additionally, similar results for the fluorescence image were observed in BTC and BCC (Figure S10b).

Furthermore, we investigated the antitumor effect of the BTC NPs and BCC NPs with or without a light trigger *in vivo*. Thirty female BALB/c mice bearing 4T1 tumors were blindly separated into six groups treated with saline, saline plus light, BCC NPs, BCC NPs plus light, BTC NPs, and BTC NPs plus light. As shown in Figure 6a, tumors grew rapidly in mice treated with saline with or without laser irradiation. A similar tumor growth tendency was displayed for mice treated with the BCC NPs or the BTC NPs but without light, showing negligible dark toxicity. However, both BTC NPs plus light and BCC NPs plus light exhibited satisfactory antitumor effects. More interestingly, BTC NPs plus light displayed better antitumor efficacy than BCC NPs plus light, revealing the combined therapeutic effect of photodynamic therapy and chemotherapy. The tumor weight (Figure 6b) and photographs (Figure 6d) also confirmed the above results. We further examined the antitumor effect of the BTC NPs by analyzing hematoxylin and eosin (H&E)-stained tumor tissues. As shown in Figure 6e, there was almost no cell necrosis or apoptosis in the group treated with saline, saline plus light, BCC NPs or BTC NPs, while a large number of shrinking and nuclear pyknosis cells appeared in the other two groups of BCC NPs plus light and BTC NPs plus light. Moreover, tumor cell proliferation seemed to be inhibited significantly in the BTC NPs plus light group.

Finally, the safety of the BTC NPs and BCC NPs were evaluated by observing the body weight change of mice under treatment and analyzing H&E-stained main organs (heart, liver, spleen, lung and kidney). The body weight of mice after BTC NPs plus light and BCC NPs plus light treatment remained stable (Figure 6c). Additionally, there were no pathological changes in the main H&E-stained organs in the BTC NPs plus light and BCC NPs plus light group (Figure S11), suggesting that no obvious toxicity or side effects were observed. Overall, the above results proved that BTC NPs had superior biocompatibility and outstanding antitumor effects with light.

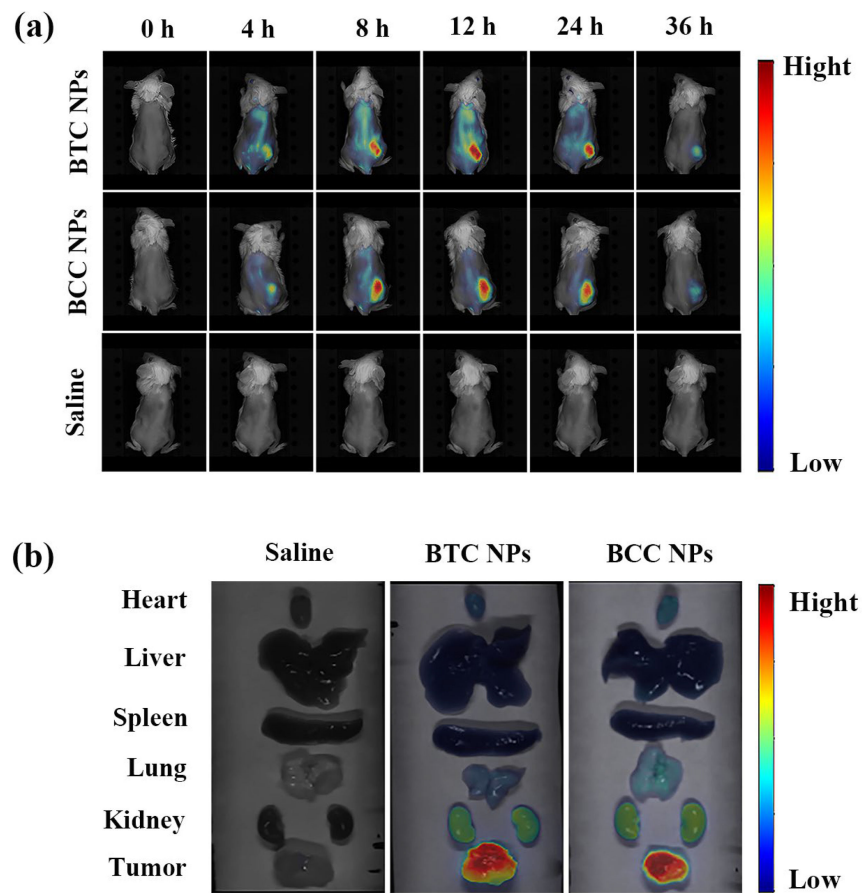


Figure 5. (a) Fluorescence images of 4T1 tumor-bearing mice at different time points after treatment with BTC NPs, BCC NPs and saline. (b) The Ex vivo fluorescence images of the different organs and tumors at 12 h after intravenous injection with BTC NPs (or BCC NPs).

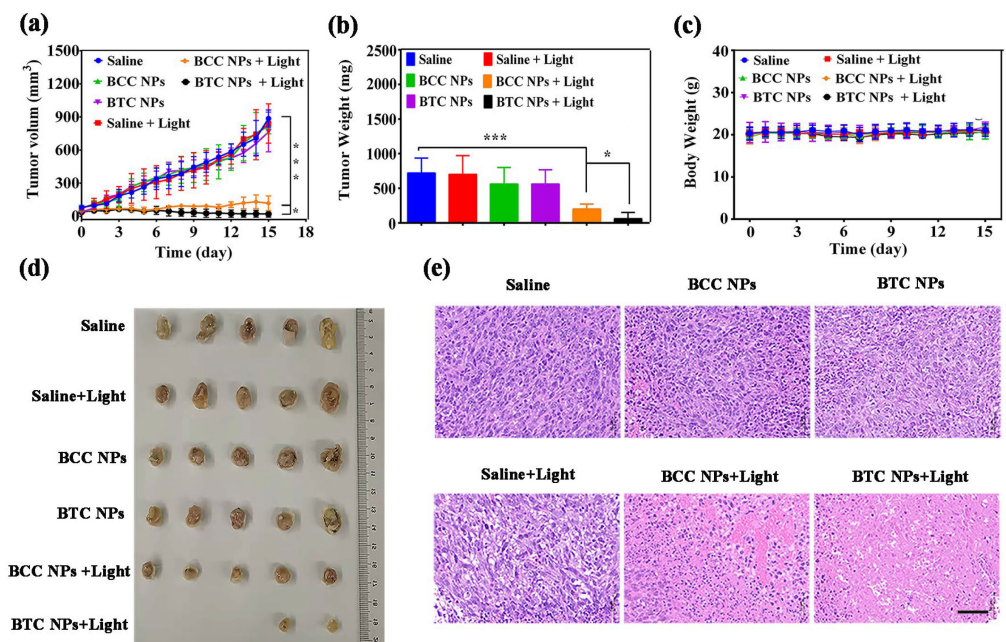


Figure 6. Antitumor effects on BALB/c mice with 4T1 tumors, (a) Tumor growth curves of BALB/c mice. (b) Weight of the tumors, (c) body weight of mice, (d) photographs of the tumors. (e) H&E staining images of tumors. (* $p < 0.05$, *** $p < 0.001$).

3. Materials and Methods

3.1. General

The purification of solvent, instrumentation, photophysical and photochemical investigations are described in the Supporting Information. Compounds **1**, **2**, **3a** and **3b** were prepared, as previously reported [48].

3.1.1. Synthesis of BTC

A solution of **2** (0.16 g, 0.12 mmol) and **3a** (21 g, 31 μ mol) in dichloromethane (6 mL) was added to a mixture of $\text{CuSO}_4 \cdot 5\text{H}_2\text{O}$ (15 mg, 60 μ mol) and sodium ascorbate (30 mg, 0.15 mmol) in water (0.5 mL). Then, 0.5 mL of ethanol was added. The resulting mixture was stirred overnight under N_2 , poured into saturated sodium chloride and extracted with dichloromethane twice (2×15 mL). The crude product was further purified by column chromatography on silica gel using dichloromethane/MeOH (50/1, *v/v*) as the eluent to produce BTC as a dark green solid. (39 mg, 65%). ^1H NMR (400 MHz, CDCl_3): δ = 8.71 (s, 1 H), 8.55 (d, *J* = 8.4 Hz, 1 H), 8.37 (s, 2 H), 8.25 (d, *J* = 8.8 Hz, 1 H), 8.18 (d, *J* = 8.8 Hz, 2 H), 8.00 (d, *J* = 16.4 Hz, 2 H), 7.90 (d, *J* = 8.4 Hz, 2 H), 7.88 (s, 2 H), 7.80 (t, *J* = 7.6 Hz, 2 H), 7.63 (t, *J* = 7.6 Hz, 2 H), 7.52 (d, *J* = 16.4 Hz, 2 H), 7.44 (d, *J* = 8.0 Hz, 2 H), 7.39 (d, *J* = 7.6 Hz, 2 H), 7.31 (s, 2 H), 7.20 (d, *J* = 8.4 Hz, 4 H), 6.90 (d, *J* = 8.4 Hz, 2 H), 5.67 (d, *J* = 17.2 Hz, 2 H), 5.36 (d, *J* = 16.8 Hz, 2 H), 5.28 (s, 4 H), 5.24 (s, 4 H), 4.57 (t, *J* = 4.8 Hz, 4 H), 4.46 (t, *J* = 5.2 Hz, 4 H), 4.27–4.20 (m, 8 H), 4.15 (t, *J* = 6.8 Hz, 4 H), 3.89 (t, *J* = 4.8 Hz, 4 H), 3.74 (t, *J* = 4.4 Hz, 4 H), 3.67–3.62 (m, 8 H), 3.52 (t, *J* = 4.0 Hz, 4 H), 3.34 (s, 6 H), 2.85 (t, *J* = 6.8 Hz, 4 H), 2.78 (t, *J* = 6.8 Hz, 4 H), 2.29–2.09 (m, 4 H), 1.50 (d, *J* = 9.2 Hz, 12 H), 1.34 (s, 6 H), 0.98 (t, *J* = 7.2 Hz, 6 H). ^{13}C NMR (100.6 MHz): δ 167.33, 157.21, 154.26, 153.44, 152.26, 151.07, 150.89, 149.58, 148.93, 148.76, 148.32, 148.06, 146.52, 145.62, 144.07, 140.38, 138.88, 136.10, 135.00, 133.94, 132.96, 131.86, 131.32, 130.79, 130.67, 130.11, 129.52, 128.45, 128.29, 128.17, 128.02, 126.63, 124.27, 123.27, 122.42, 120.63, 120.11, 116.17, 114.76, 113.99, 110.56, 95.90, 77.98, 71.89, 70.76, 70.61, 70.47, 69.57, 68.59, 67.51, 67.06, 67.04, 65.73, 63.53, 58.97, 56.57, 50.03, 48.88, 31.83, 30.87, 30.85, 28.78, 28.74, 13.87, 7.67. HRMS-ESI (*m/z*): $[\text{M}+\text{H}]^+$ calcd for $\text{C}_{121}\text{H}_{125}\text{BBBr}_2\text{F}_2\text{N}_{14}\text{O}_{35}\text{S}_5$, 2704.5549, found 2704.5558.

3.1.2. Synthesis of BCC

Similarly, **2** (0.16 g, 0.12 mmol) was treated with **3b** (21 g, 31 μ mol), $\text{CuSO}_4 \cdot 5\text{H}_2\text{O}$ (15 mg, 60 μ mol) and sodium ascorbate (30 mg, 0.15 mmol) to produce BCC as a dark green solid. (39 mg, 71%). ^1H NMR (400 MHz, CDCl_3): δ = 8.70 (s, 1 H), 8.53 (d, *J* = 8.4 Hz, 1 H), 8.38 (s, 2 H), 8.21 (d, *J* = 10.0 Hz, 1 H), 8.19 (d, *J* = 8.8 Hz, 2 H), 8.00 (d, *J* = 16.4 Hz, 2 H), 7.91 (d, *J* = 8.4 Hz, 2 H), 7.88 (s, 2 H), 7.80 (t, *J* = 7.6 Hz, 2 H), 7.64 (t, *J* = 7.6 Hz, 2 H), 7.51 (d, *J* = 16.8 Hz, 2 H), 7.43 (d, *J* = 8.0 Hz, 2 H), 7.37 (d, *J* = 8.0 Hz, 2 H), 7.32 (s, 2 H), 7.21 (d, *J* = 6.4 Hz, 4 H), 6.92 (d, *J* = 8.8 Hz, 2 H), 5.67 (d, *J* = 17.2 Hz, 2 H), 5.37 (d, *J* = 17.2 Hz, 2 H), 5.29 (s, 4 H), 5.25 (s, 4 H), 4.60 (t, *J* = 5.2 Hz, 4 H), 4.47 (t, *J* = 5.2 Hz, 4 H), 4.22 (t, *J* = 4.8 Hz, 4 H), 4.12–4.04 (m, 4 H), 4.00 (t, *J* = 6.8 Hz, 4 H), 3.90 (t, *J* = 4.8 Hz, 4 H), 3.75 (t, *J* = 4.8 Hz, 4 H), 3.66 (t, *J* = 4.8 Hz, 4 H), 3.63 (t, *J* = 4.8 Hz, 4 H), 3.52 (t, *J* = 4.4 Hz, 4 H), 3.35 (s, 6 H), 2.29–2.11 (m, 4 H), 1.66–1.54 (m, 8 H), 1.37–1.33 (m, 8 H), 1.28 (s, 6 H), 0.99 (t, *J* = 7.6 Hz, 6 H). ^{13}C NMR (100.6 MHz): δ 167.47, 157.23, 155.26, 154.54, 153.77, 152.24, 151.06, 150.86, 149.58, 148.94, 148.74, 148.35, 148.05, 146.42, 145.78, 144.11, 138.90, 136.08, 135.00, 133.92, 132.97, 131.84, 131.35, 130.76, 130.71, 130.13, 129.47, 128.51, 128.28, 128.18, 128.04, 126.60, 124.20, 123.27, 122.42, 120.61, 120.16, 116.19, 114.74, 113.98, 110.55, 95.95, 77.68, 71.88, 70.75, 70.60, 70.46, 69.56, 68.89, 68.58, 68.33, 67.02, 65.46, 63.54, 58.96, 50.00, 48.95, 31.86, 28.36, 28.32, 25.18, 13.85, 7.65. HRMS-ESI (*m/z*): $[\text{M}+\text{H}]^+$ calcd for $\text{C}_{119}\text{H}_{121}\text{BBBr}_2\text{F}_2\text{N}_{14}\text{O}_{35}\text{S}$, 2548.6353, found 2548.6357.

3.2. Photophysics and Photochemistry Investigations

3.2.1. GSH-Responsive Fluorescence Emission

GSH was dissolved in deionized water to obtain 0.5 M stock solution. BTC and BCC were dissolved in DMSO to produce 2 mM stock solutions. The samples of BTC (or BCC)

(2.5 μM) with various concentrations of GSH (0 μM , 2.5 μM , 2.5 mM) in a mixture of DMSO and PBS (*v/v*, 3:1) were then obtained. There were four groups: (1) BTC + 2.5 μM GSH; (2) BTC + 2.5 mM; (3) BCC + 2.5 μM GSH; and (4) BTC + 2.5 mM. The fluorescence emission spectra of the sample solutions were determined continuously for 2 h under excitation at 640 nm.

3.2.2. Intramolecular FRET Process Evaluation

CPT, 2, BTC and BCC were dissolved in DMSO to produce a 1 mM solution, which was then diluted to 2 μM with a mixture of DMSO and PBS (*v/v*, 3:1). The fluorescence emission spectrum of these solutions was recorded at 380–900 nm ($\lambda_{\text{ex}} = 370$ nm).

3.2.3. Photoinduced CPT Release

BTC and BCC were dissolved in DMSO to produce 2 mM stock solutions. GSH was dissolved in deionized water to obtain 0.5 M stock solution. BTC (2.5 μM) and GSH (0 μM , 2.5 μM and 2.5 mM) were prepared in a mixture of DMSO and PBS (*v/v*, 3:1) and cocultured at room temperature for 2 h. BCC was directly incubated with GSH (2.5 mM) at room temperature for 2 h. Then, the sample solution was irradiated by a 660 nm laser with a power of 30 mW/cm² for 120 min. The release of CPT was recorded by monitoring the fluorescence changes at 430 nm ($\lambda_{\text{ex}} = 370$ nm) with illumination time.

3.3. Preparation and Characterization of BTC NPs and BCC NPs

3.3.1. Preparation of BTC NPs and BCC NPs

In short, 25 mg DSPE-mPEG₂₀₀₀ was dissolved in 10 mL water and ultrasonicated for 5 min at room temperature. A solution of BTC (or BCC) (1 mM) in 100 μL DMSO was added to the DSPE-mPEG₂₀₀₀ aqueous solution by dropwise addition and stirred overnight at room temperature to stabilize and create uniform nanoparticles.

3.3.2. Characterization of BTC NPs and BCC NPs

The hydrodynamic diameters of the BTC NPs and BCC NPs were recorded by dynamic light scattering (DLS). The morphology of the BTC NPs and BCC NPs were determined by transmission electron microscopy (TEM). The stability of the BTC NPs and BCC NPs were recorded by detecting the changes in size through DLS over 7 days in phosphate-buffered saline (PBS) solution (10 μM , pH 7.4) at 37 °C.

3.4. In Vitro Studies

3.4.1. GSH-Responsive Intracellular Fluorescence

Buthionine sulfoximine (BSO) can inhibit GSH synthesis in cells. The 4T1 and MCF-7 cells (1×10^5) in 1 mL of Dulbecco's modified Eagle's medium (DMEM) were seeded and cultured in a confocal dish and incubated overnight. Then, the cells were continued to incubate with BSO (10 mM) in 1 mL DMEM medium for 12 h. Free DMEM without BSO was added to another group. After removing the old medium and rinsing three times with PBS, 1 mL DMEM medium bearing the BTC NPs and BCC NPs (5 μM) was added and incubated for 24 h. The cells were washed three times with PBS, serum-free medium was added to the dishes and intracellular fluorescence images were obtained by confocal laser scanning microscopy (CLSM). The BODIPY unit was excited at 633 nm and collected at 650–800 nm.

3.4.2. Intracellular ROS Measurement

Intracellular ROS levels of the BTC NPs and BCC NPs were detected by a DCFH-DA probe. First, 4T1 and MCF-7 cells (1×10^5) were seeded in a 12-well plate and incubated overnight at 37 °C with 5% CO₂. Then, the cells were incubated with BSO (10 mM) in 1 mL DMEM medium for 12 h. Free DMEM medium without BSO was added to another group, after removing the old DMEM medium and rinsing three times with PBS, 1 mL DMEM medium containing BTC NPs (or BCC NPs) (2 μM) was added and fresh DMEM was added

as a control. After incubation for 24 h, the old DMEM medium was removed, and the plates were rinsed thrice with PBS. The 1 mL DMEM medium bearing DCFH-DA (10 μ M) was added to each well and incubated for another 1 h. After washing three times with PBS, fresh DMEM without serum and phenol red was added and the cells were placed under 660 nm laser irradiation at 20 mW/cm² for 5 min. Moreover, flow cytometry was used to collect quantitative data on the intracellular ROS level.

3.4.3. Intracellular CPT Release

First, 4T1 and MCF-7 cells (1×10^5) in 1 mL of DMEM were seeded and cultured in a confocal dish and incubated overnight. After washing three times with PBS, 1 mL DMEM medium of the BTC NPs (or BCC NPs) (5 μ M) was added to the dish and incubated for 24 h. Meanwhile, the old medium was removed and rinsed three times with PBS. Then, 1 mL serum-free medium was added to the dishes. Subsequently, the dishes were irradiated with LED irradiation (660 nm, 20 mW/cm²) for 2 min, incubated for an additional 15 min and finally imaged by CLSM. The CPT was excited at 405 nm and detected at 425–475 nm and the BODIPY unit was excited at 633 nm and collected at 650–800 nm.

3.4.4. Photocytotoxicity Assay

MTT can detect the cytotoxicity of each compound. In short, 5000 4T1 and MCF-7 cells in 100 μ L were seeded into 96-well plates and cultured overnight. Thereafter, the old medium was removed, and the cells were cultured with free medium containing BTC NPs (or BCC NPs) at different concentrations. After 24 h of incubation, the cells were washed three times with PBS and the new DMEM medium was added. The cells were irradiated with or without a 660 nm LED lamp (20 mW/cm²) for 5 min and then cultured for another 12 h. Afterward, 10 μ L of MTT (5 mg/mL) was added to each well and cultured for 4 h. Finally, the media was discarded and 100 μ L of DMSO was added to each well. The optical density (OD) was measured at 570 nm by a microplate reader. The larger the OD value is, the stronger the cell activity. Cell viability = (OD_{sample}/OD_{control}) \times 100%.

3.4.5. Cell Apoptosis Assay

The 4T1 and MCF-7 cells were seeded into 6 wells at a density of 1×10^5 cells per well and incubated overnight. Then, BTC NPs (or BCC NPs) (5 μ M) was added for an additional 24 h. The cells were treated with a 660 nm LED lamp at 20 mW/cm² for 5 min and incubated for another 12 h. Meanwhile, the cells were collected, washed three times with PBS, and stained with PI (5 μ L) and Annexin V-FITC (15 μ L) solutions for 15 min based on the guidelines of the apoptosis kit (Beyotime Biotechnology, C1062L, Shanghai, China). Finally, the cells were placed on ice and detected by flow cytometry.

3.5. In Vivo Studies

All BALB/c mice (female, 20–25 g) were purchased from the Wushi Laboratory Animal Services Centre (Fuzhou, China). All experiments were performed according to the Institutional Animal Care and Treatment Committee of Fuzhou University. The healthy 4T1 cells were digested, centrifuged, washed twice with PBS and then collected in centrifugal tubes. Thereafter, 4T1 cells were subcutaneously injected at a density of 2×10^6 cells (100 μ L) per mouse on the right side of the back. After the average tumor size reached a certain volume (approximately 80 mm³), all animal experiments were performed.

3.5.1. In Vivo Fluorescence Imaging Study

A saline solution of BTC NPs, BCC NPs, BTC and BCC (2 mg/kg) were prepared, and 25 mice were randomly assigned to five groups (BCC NPs, BTC NPs, BCC, BTC and control). Each mouse was injected with 100 μ L of solution via the tail vein. The changes in drug fluorescence in mice were observed by using the PerkinElmer FMT2500LX imaging system at different time points (0, 4, 6, 12, 24, 36) after injection. At the time point of maximum concentration of drugs in tumor tissues, the experimental mice were euthanized,

and the heart, liver, spleen, lung and kidney were removed. A small animal imager was used to compare the drug distribution in different tissues of each group.

3.5.2. In Vivo Antitumor Assay

Thirty mice were randomly assigned to six groups: (1) saline; (2) saline plus laser; (3) BCC NPs; (4) BCC NPs plus laser; (5) BTC NPs; and (6) BTC NPs plus laser. Each group was injected with 100 μ L solution via the tail vein. Then, the mice in the (2), (4) and (6) groups were irradiated with a 660 nm laser at a power of 300 mW/cm² for 10 min. After light treatment, the mice were weighed, and the tumor volume was measured at regular times every day for 15 days.

After treatment, a mouse was randomly selected from each group and killed by the cervical dislocation method. The tumor, heart, liver, spleen, lung and kidney were removed and immersed in 4% paraformaldehyde solution for fixation for 24 h. Paraffin-wrapped sections were prepared for H&E staining. The histological morphology of each tissue section was observed and photographed under a light microscope.

4. Conclusions

In conclusion, we designed and synthesized a GSH-activatable and ROS-responsive nano-prodrug, BTC, to attain the target PDT–chemo treatment for breast cancer. The BTC NPs were dormant without chemotoxicity and phototoxicity in healthy tissues. After the BTC NPs entered the 4T1 and MCF-7 tumor cells, the DNBS group was removed and the BODIPY derivative was activated by the high concentration of GSH. Subsequently, BTC NPs generated ROS after irradiation, and then the ROS cleaved the ROS-cleavable TK linkage to realize on-demand CPT release. The IC₅₀ values for the BTC NPs were 0.50 μ M toward 4T1 cells and 0.63 μ M against MCF-7 cells, showing strong photocytotoxicities to tumor cells. The BTC NPs have been proven to have efficient tumor-targeting and tumor-suppressive effects without obvious toxicity and side effects in 4T1 tumor-bearing mice, which is of great significance for cancer treatment.

Supplementary Materials: The supporting information can be downloaded at: <https://www.mdpi.com/article/10.3390/ijms232415656/s1>.

Author Contributions: J.L., Q.L., L.C. and Z.L. designed the experiments; Z.L. and G.X. performed the experiments and prepared the manuscript; X.Y., S.L. and Y.S. participated in part of the experiments; J.L. and Q.L. revised the paper and supervised the whole process. All authors have read and agreed to the published version of the manuscript.

Funding: This study was funded by the National Natural Science Foundation of China (81873045, 21471033), The Natural Science Foundation of Fujian Province, China (2020J011118, 2020J011115, 2021J01608, 2020J01440), Fujian Province Health Care Young and Middle-aged Backbone Talents Training Project (2020GGA015), Startup Fund for Scientific Research, Fujian Medical University (2020QH1225), Excellent Young Talents Training Plan of Fujian Cancer Hospital (2020YNYQ01), Fujian Provincial Clinical Research Center for Cancer Radiotherapy and Immunotherapy (2020Y2012), The Fuzhou University Testing Fund of Precious Apparatus (No. 2022T041).

Institutional Review Board Statement: Not applicable.

Informed Consent Statement: Not applicable.

Data Availability Statement: Not applicable.

Conflicts of Interest: The authors declare that they have no known competing financial interests or personal relationships that could have appeared to influence the work reported in this paper.

References

1. Michael, M.D.; Louise, L.J. The Role of Inflammation in Progression of Breast Cancer: Friend or Foe? (Review). *Int. J. Oncol.* **2015**, *47*, 797–805. [[CrossRef](#)]
2. Cai, Y.; Wang, B.; Li, B.; Huang, X.; Guo, H.; Liu, Y.; Chen, B.; Zhao, S.; Wu, S.; Li, W.; et al. Collection on Reports of Molecules Linked to Epithelial-Mesenchymal Transition in the Process of Treating Metastasizing Cancer: A Narrative Review. *Ann. Transl. Med.* **2021**, *9*, 946. [[CrossRef](#)] [[PubMed](#)]
3. Sakaue-Sawano, A.; Kobayashi, T.; Ohtawa, K.; Miyawaki, A. Drug-induced Cell Cycle Modulation Leading to Cell-cycle Arrest, Nuclear Mis-segregation, or Endoreplication. *BMC Cell Biol.* **2011**, *12*, 2. [[CrossRef](#)] [[PubMed](#)]
4. Su, Z.; Dong, S.; Zhao, S.; Liu, K.; Tan, Y.; Jiang, X.; Assaraf, Y.; Qin, B.; Chen, Z.; Zou, C. Novel Nanomedicines to Overcome Cancer Multidrug Resistance. *Drug Resist. Updates* **2021**, *58*, 100777. [[CrossRef](#)] [[PubMed](#)]
5. Chudy, M.; Tokarska, K.; Jastrzebska, E.; Bułka, M.; Drozdek, S.; Lamch, Ł.; Wilk, K.; Brzózka, Z. Lab-on-a-chip Systems for Photodynamic Therapy Investigations. *Biosens. Bioelectron.* **2018**, *101*, 37–51. [[CrossRef](#)] [[PubMed](#)]
6. Cheng, X.; Gao, J.; Ding, Y.; Lu, Y.; Wei, Q.; Cui, D.; Fan, J.; Li, X.; Zhu, E.; Lu, Y.; et al. Multi-Functional Liposome: A Powerful Theranostic Nano-Platform Enhancing Photodynamic Therapy. *Adv. Sci.* **2021**, *8*, 2100876. [[CrossRef](#)]
7. Wan, Y.; Fu, L.; Li, C.; Lin, J.; Huang, P. Conquering the Hypoxia Limitation for Photodynamic Therapy. *Adv. Mater.* **2021**, *33*, 2103978. [[CrossRef](#)]
8. Zhuang, Z.; Dai, J.; Yu, M.; Li, J.; Shen, P.; Hu, R.; Lou, X.; Zhao, Z.; Tang, B. Type I Photosensitizers Based on Phosphindole Oxide for Photodynamic Therapy: Apoptosis and Autophagy Induced by Endoplasmic Reticulum Stress. *Chem. Sci.* **2020**, *11*, 3405–3417. [[CrossRef](#)]
9. Zhang, L.; Ding, D. Recent Advances of Transition Ir(III) Complexes as Photosensitizers for Improved Photodynamic Therapy. *VIEW* **2021**, *2*, 20200179. [[CrossRef](#)]
10. Majerník, M.; Jendželovský, R.; Vargová, J.; Jendželovská, Z.; Fedoročko, P. Multifunctional Nanoplatfroms as A Novel Effective Approach in Photodynamic Therapy and Chemotherapy, to Overcome Multidrug Resistance in Cancer. *Pharmaceutics* **2022**, *14*, 1075. [[CrossRef](#)]
11. Alves, S.; Calori, I.; Tedesco, A. Photosensitizer-based Metal-organic Frameworks for Highly Effective Photodynamic Therapy. *Mater. Sci. Eng. C Mater. Biol. Appl.* **2021**, *131*, 112514. [[CrossRef](#)]
12. Nishiyama, N.; Morimoto, Y.; Jang, W.; Kataoka, K. Design and Development of Dendrimer Photosensitizer-incorporated Polymeric Micelles for Enhanced Photodynamic Therapy. *Adv. Drug Deliv. Rev.* **2009**, *61*, 327–338. [[CrossRef](#)]
13. Brown, J.M. Tumor Microenvironment and the Response to Anticancer Therapy. *Cancer Biol. Ther.* **2002**, *1*, 453–458. [[CrossRef](#)]
14. Wiese, M.; Stefan, S.M. The A-B-C of Small-molecule ABC Transport Protein Modulators: From Inhibition to Activation—A Case Study of Multidrug Resistance-associated Protein 1 (ABCC1). *Med. Res. Rev.* **2019**, *39*, 2031–2081. [[CrossRef](#)]
15. Hao, Y.; Chen, Y.W.; He, X.; Yu, Y.; Han, R.; Li, Y.; Yang, C.; Hu, D.; Qian, Z. Polymeric Nanoparticles with ROS-responsive Prodrug and Platinum Nanozyme for Enhanced Chemophotodynamic Therapy of Colon Cancer. *Adv. Sci.* **2020**, *7*, 2001853. [[CrossRef](#)]
16. Liu, L.; Qiu, W.; Li, B.; Zhang, C.; Sun, L.; Wan, S.; Rong, L.; Zhang, X. A Red Light Activatable Multifunctional Prodrug for Image-guided Photodynamic Therapy and Cascaded Chemotherapy. *Adv. Funct. Mater.* **2016**, *26*, 6257–6269. [[CrossRef](#)]
17. Yang, C.; Wen, F.; Du, Y.; Luo, M.; Lu, Y.; Liu, Y.; Lin, H. A Hypoxia-Activated Prodrug Conjugated with a BODIPY-Based Photothermal Agent for Imaging-Guided Chemo-Photothermal Combination Therapy. *ACS Appl. Mater.* **2022**, *14*, 40546–40558. [[CrossRef](#)]
18. Tam, L.K.B.; Yu, L.; Wong, R.C.H.; Fong, W.P.; Ng, D.K.P.; Lo, P.C. Dual Cathepsin and Glutathione-Activated Dimeric and Trimeric Phthalocyanine-Based Photodynamic Molecular Beacons for Targeted Photodynamic Therapy. *J. Med. Chem.* **2021**, *64*, 17455–17467. [[CrossRef](#)]
19. Yu, Z.; Wang, H.; Chen, Z.; Dong, X.; Zhao, W.; Shi, Y.; Zhu, Q. Discovery of an Amino Acid-Modified Near-Infrared Aza-BODIPY Photosensitizer as an Immune Initiator for Potent Photodynamic Therapy in Melanoma. *J. Med. Chem.* **2022**, *65*, 3616–3631. [[CrossRef](#)]
20. Chu, D.; Dong, X.; Zhao, Q.; Gu, J.; Wang, Z. Photosensitization Priming of Tumor Microenvironments Improves Delivery of Nanotherapeutics via Neutrophil Infiltration. *Adv. Mater.* **2017**, *29*, 1701021. [[CrossRef](#)]
21. Wang, X.; Wang, X.; Jin, S.; Muhammad, N.; Guo, Z. Stimuli-Responsive Therapeutic Metalloodrugs. *Chem. Rev.* **2019**, *119*, 1138–1192. [[CrossRef](#)] [[PubMed](#)]
22. Gasser, S.; Lim, L.H.K.; Cheung, F.S.G. The Role of the Tumour Microenvironment in Immunotherapy. *Endocr. Relat. Cancer* **2017**, *24*, T283–T295. [[CrossRef](#)] [[PubMed](#)]
23. Huai, Y.; Hossen, M.N.; Wilhelm, S.; Bhattacharya, R.; Mukherjee, P. Nanoparticle Interactions with the Tumor Microenvironment. *Bioconjug. Chem.* **2019**, *30*, 2247–2263. [[CrossRef](#)] [[PubMed](#)]
24. Ha, S.; Zou, Y.; Fong, W.; Ng, D.K.P. Multifunctional Molecular Therapeutic Agent for Targeted and Controlled Dual Chemo-and Photodynamic Therapy. *J. Med. Chem.* **2020**, *63*, 8512–8523. [[CrossRef](#)]
25. Ihsanullah, K.M.; Kumar, B.N.; Zhao, Y.; Muhammad, H.; Liu, Y.; Wang, L.; Liu, H.; Jiang, W. Stepwise-Activatable Hypoxia Triggered Nanocarrier-Based Photodynamic Therapy for Effective Synergistic Bioreductive Chemotherapy. *Biomaterials* **2020**, *245*, 119982. [[CrossRef](#)] [[PubMed](#)]

26. Pan, W.; Tan, Y.; Meng, W.; Huang, N.; Zhao, Y.; Yu, Z.; Huang, Z.; Zhang, W.; Sun, B.; Chen, J. Microenvironment-Driven Sequential Ferroptosis, Photodynamic Therapy, and Chemotherapy for Targeted Breast Cancer Therapy by a Cancer-Cell-Membrane-Coated Nanoscale Metal-Organic Framework. *Biomaterials* **2022**, *282*, 121449. [[CrossRef](#)]
27. James, N.S.; Joshi, P.; Ohulchanskyy, T.Y.; Chen, Y.; Tabaczynski, W.; Durrani, F.; Shibata, M.; Pandey, R.K. Photosensitizer (PS)-Cyanine Dye (CD) Conjugates: Impact of the Linkers Joining the PS and CD Moieties and Their Orientation in Tumor-Uptake and Photodynamic Therapy (PDT). *Eur. J. Med. Chem.* **2016**, *122*, 770–785. [[CrossRef](#)]
28. Wu, X.; Wu, W.; Cui, X.; Zhao, J.; Wu, M. Preparation of Bodipy–ferrocene Dyads and Modulation of the Singlet/Triplet Excited State of Bodipy via Electron Transfer and Triplet Energy Transfer. *J. Mater. Chem. C Mater.* **2016**, *4*, 2843–2853. [[CrossRef](#)]
29. Bio, M.; Rajaputra, P.; You, Y. Photodynamic Therapy via FRET Following Bioorthogonal Click Reaction in Cancer Cells. *Bioorg. Med. Chem. Lett.* **2016**, *26*, 145–148. [[CrossRef](#)]
30. Yang, G.; Sun, X.; Liu, J.; Feng, L.; Liu, Z. Light-Responsive, Singlet-Oxygen-Triggered On-Demand Drug Release from Photosensitizer-Doped Mesoporous Silica Nanorods for Cancer Combination Therapy. *Adv. Funct. Mater.* **2016**, *26*, 4722–4732. [[CrossRef](#)]
31. Sasan, S.; Chopra, T.; Gupta, A.; Tsering, D.; Kapoor, K.K.; Parkesh, R. Fluorescence “turn-off” and Colorimetric Sensor for Fe²⁺, Fe³⁺, and Cu²⁺ Ions Based on a 2,5,7-Triarylimidazopyridine Scaffold. *ACS Omega* **2022**, *7*, 11114–11125. [[CrossRef](#)]
32. Thapa, P.; Li, M.; Bio, M.; Rajaputra, P.; Nkepeng, G.; Sun, Y.; Woo, S.; You, Y. Far-Red Light-Activatable Prodrug of Paclitaxel for the Combined Effects of Photodynamic Therapy and Site-Specific Paclitaxel Chemotherapy. *J. Med. Chem.* **2016**, *59*, 3204–3214. [[CrossRef](#)]
33. Turan, I.S.; Cakmak, F.P.; Yildirim, D.C.; Cetin-Atalay, R.; Akkaya, E.U. Near-IR Absorbing BODIPY Derivatives as Glutathione-Activated Photosensitizers for Selective Photodynamic Action. *Chemistry* **2014**, *20*, 16088–16092. [[CrossRef](#)]
34. Zheng, G.; Chen, J.; Stefflova, K.; Jarvi, M.; Li, H.; Wilson, B.C. Photodynamic Molecular Beacon as an Activatable Photosensitizer Based on Protease-Controlled Singlet Oxygen Quenching and Activation. *Proc. Natl. Acad. Sci. USA* **2007**, *104*, 8989–8994. [[CrossRef](#)]
35. Huang, L.; Yang, W.; Zhao, J. Switching of the Triplet Excited State of Styryl 2,6-Diiodo-Bodipy and its Application in Acid-Activatable Singlet Oxygen Photosensitizing. *J. Org. Chem.* **2014**, *79*, 10240–10255. [[CrossRef](#)]
36. Deng, C.; Liu, Y.; Zhou, F.; Wu, M.; Zhang, Q.; Yi, D.; Yuan, W.; Wang, Y. Engineering of Dendritic Mesoporous Silica Nanoparticles for Efficient Delivery of Water-Insoluble Paclitaxel in Cancer Therapy. *J. Colloid Interface Sci.* **2021**, *593*, 424–433. [[CrossRef](#)]
37. Harmatys, K.M.; Overchuk, M.; Chen, J.; Ding, L.; Chen, Y.; Pomper, M.G.; Zheng, G. Tuning Pharmacokinetics to Improve Tumor Accumulation of a Prostate-Specific Membrane Antigen-Targeted Phototheranostic Agent. *Bioconjug. Chem.* **2018**, *29*, 3746–3756. [[CrossRef](#)]
38. Gulzar, A.; Xu, J.; Wang, C.; He, F.; Yang, D.; Gai, S.; Yang, P.; Lin, J.; Jin, D.; Xing, B. Tumour Microenvironment Responsive Nanoconstructs for Cancer Theranostic. *Nano Today* **2019**, *26*, 16–56. [[CrossRef](#)]
39. Li, M.; Cui, X.; Wei, F.; Wang, Z.; Han, X. Red Blood Cell Membrane-Coated Biomimetic Upconversion Nanoarchitectures for Synergistic Chemo-photodynamic Therapy. *New J. Chem.* **2021**, *45*, 22269–22279. [[CrossRef](#)]
40. Meng, X.; Wang, J.; Zhou, J.; Tian, Q.; Qie, B.; Zhou, G.; Duan, W.; Zhu, Y. Tumor Cell Membrane-Based Peptide Delivery System Targeting the Tumor Microenvironment for Cancer Immunotherapy and Diagnosis. *Acta Biomater.* **2021**, *127*, 266–275. [[CrossRef](#)]
41. Fu, X.; Yin, W.; Shi, D.; Yang, Y.; He, S.; Hai, J.; Hou, Z.; Fan, Z.; Zhang, D. Shuttle-shape Carrier-Free Platinum-Coordinated Nanoreactors with O₂ Self-supply and ROS Augment for Enhanced Phototherapy of Hypoxic Tumor. *ACS Appl. Mater.* **2021**, *13*, 32690–32702. [[CrossRef](#)]
42. Zhang, H.; Lin, H.; Su, D.; Yang, D.; Liu, J. Enzyme-activated Multifunctional Prodrug Combining Site-specific Chemotherapy with Light-triggered Photodynamic therapy. *Mol. Pharm.* **2022**, *19*, 630–641. [[CrossRef](#)] [[PubMed](#)]
43. Chu, D.; Dong, X.; Shi, X.; Zhang, C.; Wang, Z. Neutrophil-based Drug Delivery Systems. *Adv. Mater.* **2018**, *30*, 1706245. [[CrossRef](#)] [[PubMed](#)]
44. Chen, Y.; Xu, Z.; Zhu, D.; Tao, X.; Gao, Y.; Zhu, H.; Mao, Z.; Ling, J. Gold Nanoparticles Coated with Polysarcosine Brushes to Enhance their Colloidal Stability and Circulation Time in vivo. *J. Colloid Interface Sci.* **2016**, *483*, 201–210. [[CrossRef](#)] [[PubMed](#)]
45. Wang, X.; Luo, D.; Basilion, J.P. Photodynamic Therapy: Targeting Cancer Biomarkers for the Treatment of Cancers. *Cancers* **2021**, *13*, 2992. [[CrossRef](#)]
46. Chen, Y.; Zhang, X.; Cheng, D.; Zhang, Y.; Liu, Y.; Ji, L.; Guo, R.; Chen, H.; Ren, X.; Chen, Z.; et al. Near-infrared Laser-triggered in Situ Dimorphic transformation of BF₂-azadipyromethene Nanoaggregates for Enhanced Solid Tumor Penetration. *ACS Nano* **2020**, *14*, 3640–3650. [[CrossRef](#)]
47. Zhu, J.; Jiao, A.; Li, Q.; Lv, X.; Wang, X.; Song, X.; Li, B.; Zhang, Y.; Dong, X.C. Mitochondrial Ca²⁺-overloading by Oxygen/Glutathione Depletion-Boosted Photodynamic Therapy Based on a CaCO₃ Nanoplatform for Tumor Synergistic Therapy. *Acta Biomater.* **2022**, *137*, 252–261. [[CrossRef](#)]
48. Xu, G.; Zhang, H.; Li, X.; Yang, D.; Liu, J. Red light Triggered Photodynamic-Chemo Combination Therapy Using a Prodrug Caged by Photosensitizer. *Eur. J. Med. Chem.* **2021**, *2015*, 113251. [[CrossRef](#)]